Searching for Compact Obscured Nuclei in Compton-thick Active Galactic Nuclei

The Astrophysical Journal, 985:259 (16pp), 2025 June 1 https://doi.org/10.3847/1538-4357/adcecb

Searching for Compact Obscured Nuclei in Compton-thick Active Galactic Nuclei

Makoto A. Johnstone[1,2,14], George C. Privon[1,3,4], Loreto Barcos-Muñoz[1,3], A.S. Evans[1,3], S. Aalto[5], Lee Armus[6], Franz E. Bauer[2,7], L. Blecha[8], J. S. Gallagher[9,10], S. König[5], Claudio Ricci[11,12], Ezequiel Treister[2], Cosima Eibensteiner[3,13], Kimberly L. Emig[3], Kara N. Green[1], Devaky Kunneriath[3], Jaya Nagarajan-Swenson[1], Alejandro Saravia[1], and Ilsang Yoon[3]

[1] Department of Astronomy, University of Virginia, 530 McCormick Road, Charlottesville, VA 22903, USA
[2] Instituto de Astrofísica, Facultad de Física, Pontificia Universidad Católica de Chile, Campus San Joaquín, Av. Vicuña Mackenna 4860, Macul Santiago, 7820436, Chile
[3] National Radio Astronomy Observatory, 520 Edgemont Road, Charlottesville, VA 22903, USA
[4] Department of Astronomy, University of Florida, P.O. Box 112055, Gainesville, FL 32611, USA
[5] Department of Space, Earth and Environment, Onsala Space Observatory, Chalmers University of Technology, 43992 Onsala, Sweden
[6] IPAC, California Institute of Technology, 1200 East California Boulevard, Pasadena, CA 91125, USA
[7] Millennium Institute of Astrophysics, Nuncio Monseñor Sótero Sanz 100, Of 104, Providencia, Santiago, Chile
[8] Department of Physics, University of Florida, 2001 Museum Rd., Gainesville, FL 32611, USA
[9] Department of Astronomy, University of Wisconsin-Madison, 475 N Charter Street, Madison, WI 53706, USA
[10] Department of Physics and Astronomy, Macalester College, 1600 Grand Abe, St. Paul, MN 55105, USA
[11] Instituto de Estudios Astrofísicos, Facultad de Ingeniería y Ciencias, Universidad Diego Portales, Avenida Ejercito Libertador 441, Santiago, Chile
[12] Kavli Institute for Astronomy and Astrophysics, Peking University, Beijing 100871, People's Republic of China
Received 2024 September 24; revised 2025 April 3; accepted 2025 April 16; published 2025 May 29

Abstract

Compact obscured nuclei (CONs) are heavily obscured infrared cores that have been found in local (ultra-) luminous infrared galaxies. They show bright emission from vibrationally excited rotational transitions of HCN, known as HCN-vib, and are thought to harbor Compton-thick (CT, $N_{\rm H} \geqslant 10^{24}\ {\rm cm}^{-2}$) active galactic nuclei (AGNs) or extreme compact starbursts. We explore the potential evolutionary link between CONs and CT-AGNs by searching for CONs in hard-X-ray-confirmed CT-AGNs from the Great Observatories All-sky LIRG Survey (GOALS). Here, we present new Atacama Large Millimeter/submillimeter Array Band 6 observations that targeted HCN-vib emission in four hard-X-ray-confirmed CT-AGNs. We analyze these objects together with literature HCN-vib measurements of five additional hard-X-ray-confirmed CT-AGNs from the GOALS sample. We do not detect any CONs in this combined sample of nine CT-AGNs. We then explore a proposed evolutionary sequence in which CONs evolve into X-ray-detectable CT-AGNs once outflows and feedback reduce the column densities of the enshrouding gas. We find, however, no evidence of well-developed dense molecular outflows in the observed CT-AGNs. While this could suggest that CT-AGNs are not universally linked to CONs, it could also be explained by a short duty cycle for molecular outflows.

Unified Astronomy Thesaurus concepts: Active galactic nuclei (16); Active galaxies (17); Jets (870); Galaxy nuclei (609); Molecular gas (1073)

1. Introduction

Recent Atacama Large Millimeter/submillimeter Array (ALMA) observations have revealed deeply embedded hot ($T_{\rm dust} > 100$ K) infrared cores ($r < 100$ pc) in some local (ultra-) luminous infrared galaxies (U/LIRGs; K. Sakamoto et al. 2010; M. Imanishi & K. Nakanishi 2013; S. Aalto et al. 2015a; S. Martín et al. 2016; N. Falstad et al. 2021). These compact obscured nuclei (CONs) are characterized by a strong mid-infrared radiation field that is formed via the radiative trapping of 14 μm continuum photons by large molecular gas columns ($N_H > 10^{24}\ {\rm cm}^{-2}$; E. González-Alfonso & K. Sakamoto 2019; N. Falstad et al. 2021). Such radiation fields could be powered by either nuclear starbursts or active galactic nuclei (AGNs; B. H. Andrews & T. A. Thompson 2011; S. Aalto et al. 2015a; E. González-Alfonso & K. Sakamoto 2019), but the exact power source is unknown. Unveiling the central engine of CONs thus remains a fundamental question in understanding the nature of these infrared cores. A "starburst scenario" would require an extremely top-heavy initial mass function (IMF), consisting of mostly massive O stars (S. Aalto et al. 2019). An "AGN scenario," on the other hand, implies the presence of a Compton-thick (CT, $N_{\rm H} \geqslant 10^{24}\ {\rm cm}^{-2}$) AGN due to the obscured nature of these systems (S. Aalto et al. 2015a, 2019).

The mechanisms that drive the buildup of this nuclear obscuration are still unclear. CONs have been identified in major mergers, minor mergers, and isolated galaxies (N. Falstad et al. 2021), suggesting that both internal and interaction-driven processes can be responsible for their extreme column densities (N. Falstad et al. 2021). There are, however, striking differences in the rate of occurrence of CONs based on the infrared luminosity of the host galaxy (N. Falstad et al. 2021). In fact, N. Falstad et al. (2021) found that ∼40% of local ULIRGs ($L_{\rm IR} \geqslant 10^{12}\ L_\odot$) and ∼20% of local LIRGs ($10^{11} L_\odot \leqslant L_{\rm IR} < 10^{12}\ L_\odot$) host CONs, whereas no CONs have been identified in local lower-luminosity galaxies ($L_{\rm IR} < 10^{11}\ L_\odot$). This luminosity dependence makes U/LIRGs the only known hosts of the CON phenomenon.

[13] Jansky Fellow of the National Radio Astronomy Observatory.
[14] Corresponding author.

Optically thick layers of dust and gas pose an observational challenge when studying CONs. Interpreting spectral-line emission often proves to be difficult due to absorption from foreground layers of obscuring gas (e.g., S. Aalto et al. 2015a, 2019). The greenhouse effects of the H_2 columns, however, create a high-column-density ($N_H > 2 \times 10^{23}\,cm^{-2}$) and high-brightness-temperature ($T_b \sim 100$ K) environment that can vibrationally excite ($v_2 = 1f$) rotational transitions of HCN (3–2) (hereafter HCN-vib) via radiative pumping (L. M. Ziurys & B. E. Turner 1986; E. González-Alfonso & K. Sakamoto 2019). Bright HCN-vib emission therefore indicates the presence of a CON-like infrared core, making it a crucial tool in identifying and characterizing CONs.

Though it is unclear whether CONs harbor CT-AGNs, there are uncanny similarities in their properties. In addition to their similarly high column densities ($N_H > 10^{24}\,cm^{-2}$; E. González-Alfonso & K. Sakamoto 2019) and high bolometric luminosities (E. González-Alfonso & K. Sakamoto 2019; C. Ricci et al. 2021), both CONs and CT-AGNs have high rates of occurrence in local U/LIRGs (C. Ricci et al. 2017a; N. Falstad et al. 2021; C. Ricci et al. 2021). It is therefore possible that CONs and CT-AGNs are manifestations of the same phenomenon (that is, an obscured actively growing supermassive black hole), but their relationship is yet to be systematically studied.

Mechanical-feedback-based theories suggest that the outflow properties of CONs may give insight into their connection to CT-AGNs. For example, though many U/LIRGs have fast far-infrared OH outflows (S. Veilleux et al. 2013), CONs are notably missing them (N. Falstad et al. 2019). Instead, they host compact molecular outflows that have been detected at submillimeter wavelengths (S. García-Burillo et al. 2015; M. Pereira-Santaella et al. 2016, 2018; L. Barcos-Muñoz et al. 2018; N. Falstad et al. 2018, 2021; A. Fluetsch et al. 2019; D. Lutz et al. 2020). At least three of these molecular outflows have confirmed collimated morphologies that are reminiscent of the molecular jets seen in young stellar objects (e.g., A. L. Plunkett et al. 2015): Arp 220W (L. Barcos-Muñoz et al. 2018), ESO 320-G030 (M. Pereira-Santaella et al. 2016; M. D. Gorski et al. 2024), and Zw 049.057 (N. Falstad et al. 2018).

These unique properties motivate the theory that CONs harbor hidden CT-AGNs that evolve into X-ray-detectable CT-AGNs as their active feedback mechanisms develop. The high column densities of CONs generally preclude the X-ray detection of any AGNs that might be present. As their molecular outflows evolve and widen, however, they would sweep or erode away a fraction of the obscuring gas, creating lower-column-density sight lines through which the CON-like mid-infrared radiation field would leak out (E. González-Alfonso et al. 2017; N. Falstad et al. 2019, 2021). Once the line-of-sight column density has been reduced to orders of $N_H = 10^{24}$–$10^{25}\,cm^{-2}$, the CT-AGNs would be X-ray detectable, but the greenhouse-like conditions necessary to excite HCN-vib molecules may no longer be present (E. González-Alfonso & K. Sakamoto 2019). If the AGN bolometric luminosity remains high, the molecular outflow is expected to continue its expansion or even increase in velocity due to the loss of mass in the nuclear interstellar medium which was previously slowing the outflow's expansion. CT-AGNs following this proposed sequence may be missing CON-like HCN-vib emission, but they would have well-developed molecular outflows. In this work, we investigate this evolutionary scenario by searching for evolved molecular outflows in CT-AGNs.

In this paper, we analyze a sample of nine hard-X-ray-confirmed CT-AGNs, in which we present four new Band 6 ALMA HCN-vib observations and use archival measurements for five additional sources. We study the relationship between CT-AGNs and CONs, their distinctive properties, and their potential evolutionary connections. In Section 2, we report the sample selection process, the observational setup, and the data reduction procedure. In Section 3, we examine the HCN-vib line intensity and the kinematics of the dense gas tracers HCN (3–2) and HCO^+ (3–2). In Section 4, we discuss the potential connection between CT-AGNs and CONs. We conclude our findings in Section 5.

2. Sample and Observations

2.1. Sample

We study the prevalence of CONs in CT-AGNs ($N_H \geqslant 10^{24}\,cm^{-2}$) by analyzing observations of HCN-vib (rest frequency = 267.199 GHz for $J = 3 - 2 v_2 = 1f$). Since the CON phenomenon has only been identified in U/LIRGs and appears to have a strong luminosity dependence, we specifically target CT-AGNs in U/LIRGs. In the Great Observatories All-sky LIRG Survey (GOALS) sample (L. Armus et al. 2009), 14 CT-AGNs have been identified via NuSTAR hard X-ray observations (F. E. Bauer et al. 2015; S. H. Teng et al. 2015; C. Ricci et al. 2016, 2017b, 2021; P. Gandhi et al. 2017; S. Oda et al. 2017; K. Iwasawa et al. 2020; S. Yamada et al. 2020). Of these, five had preexisting millimeter-wave ALMA observations of HCN-vib (NGC 1068, IRAS 13120–5453, NGC 5135, NGC 6240N, and NGC 6240S; M. Imanishi et al. 2016, 2020; G. C. Privon et al. 2017; N. Falstad et al. 2021; Y. Nishimura et al. 2024). We also conducted new ALMA observations of four additional CT-AGNs from the GOALS sample (NGC 4922N, NGC 6921, NGC 7130, and NGC 7674). These objects were selected due to their visibility to ALMA (decl. $< 40°$) and lack of prior HCN-vib observations. Combined with the preexisting observations, this results in a total sample of nine CT-AGNs. The properties of these nine sources are reported in Table 1.

Previous studies used the ratio of the HCN-vib luminosity to the total infrared luminosity of the host galaxy to identify CONs with a fiducial value of $L_{HCN\text{-}vib}/L_{IR} > 10^{-8}$ (S. Aalto et al. 2015a; N. Falstad et al. 2019). N. Falstad et al. (2021), however, suggested that this criterion may be biased against galaxies with a spatially extended infrared emission region or multiple nuclei. In accordance with N. Falstad et al. (2021), we adopt an alternative fiducial value of an HCN-vib surface brightness $\Sigma_{HCN\text{-}vib} \geqslant 1\ L_\odot\,pc^{-2}$ over a spatial region of $r > 5$ pc as the detection criterion for CONs. This fiducial value is purely empirical and was selected for observations with angular resolutions of $0''.2$–$0''.8$ (∼5–100 pc; N. Falstad et al. 2021). Note that while our analysis emphasizes this $\Sigma_{HCN\text{-}vib}$ definition for CONs, we return to consider the $L_{HCN\text{-}vib}/L_{IR}$ for completeness in Section 4.1.1.

2.2. New ALMA Observations

New ALMA 12 m Array Band 6 observations of four CT-AGNs (NGC 4922N, NGC 6921, NGC 7130, and NGC 7674) were conducted as a part of Project #2017.1.00598.S (PI: Privon, G.C.). The approximate ALMA Band 6 field of view

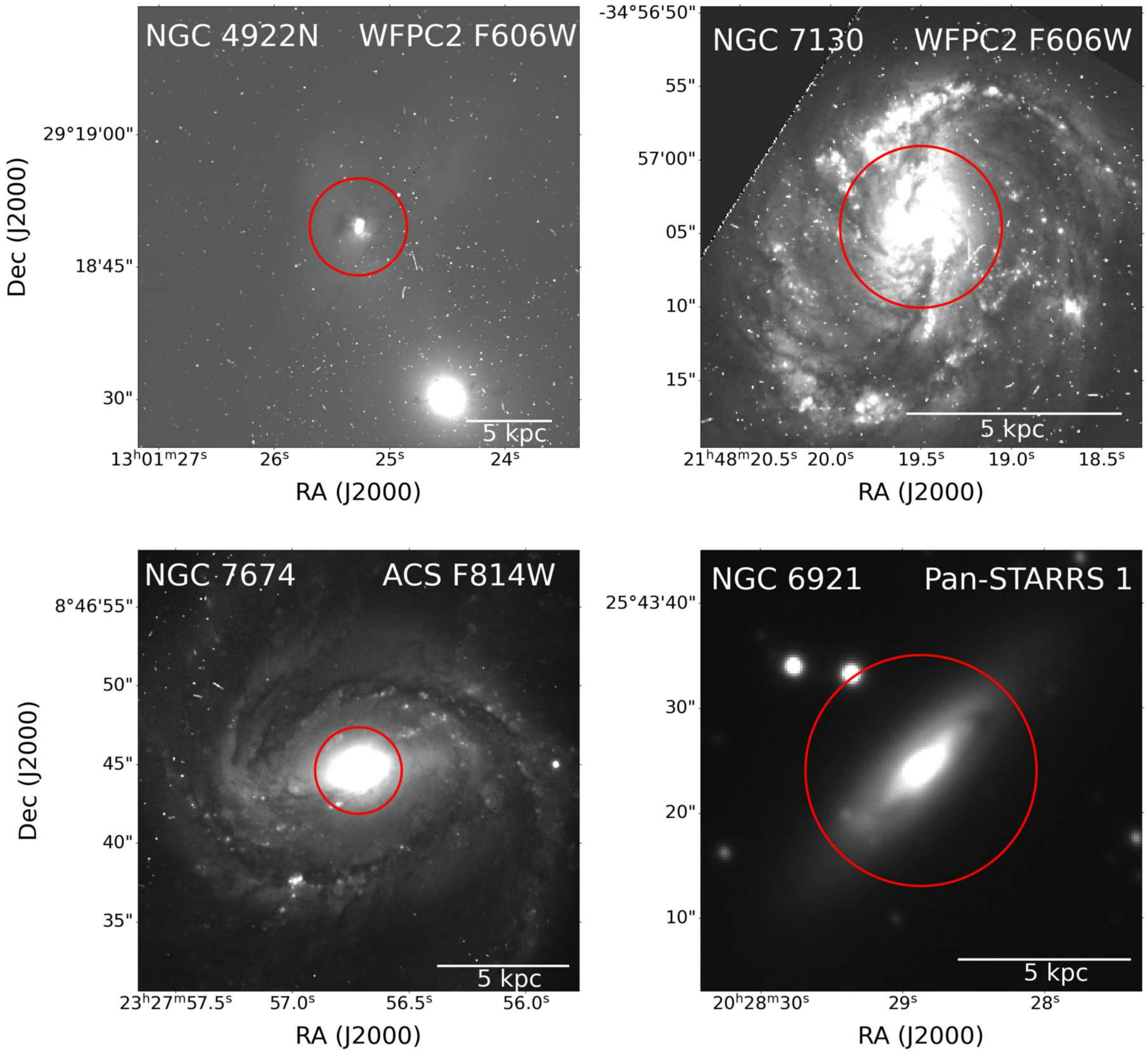

Figure 1. Optical Hubble Space Telescope (HST) or Pan-STARRS1 images of the four CT-AGNs in local U/LIRGs with new observations in our sample. The approximately Band 6 ALMA field of view (∼22″) is overlaid in red. HST images are from the following proposal IDs: 5479 (NGC 4922N, NGC 7130) and 10592 (NGC 7674). The NGC 6921 Pan-STARRS1 image is from project ID 1918.

Table 1
CT-AGNs Studied in This Work

IRAS Name	Source	z	D_L (Mpc)	$\log(L_{\rm IR}/L_\odot)$	$\log N_{\rm H}$ (cm^{-2})	f_{25}/f_{60}
F02401–0013	NGC 1068	0.0038	15.9	11.40	⩾24.99	0.448
F12590+2934	NGC 4922N[a]	0.0232	111.0	11.38	25.10 [24.63-NC]	0.195
13120–5453	⋯	0.0308	144.0	12.32	24.50 [24.27–24.74]	0.072
F13229–2934	NGC 5135	0.0137	60.9	11.30	24.80 [24.51–25.00]	0.141
F16504+0228	NGC 6240N	0.0245	116.0	11.93	24.19 [24.09–24.36]	0.155
F16504+0228	NGC 6240S	0.0245	116.0	11.93	24.17 [24.11–24.23]	0.155
20264+2533	NGC 6921[a]	0.0139	64.2	11.11	24.15 [23.83–24.40]	0.358
F21453–3511	NGC 7130[a]	0.0162	72.7	11.42	24.61 [24.50–24.66]	0.055
F23254+0830	NGC 7674[a]	0.0289	125.0	11.56	⩾24.48	0.129

Note. NC: value not constrained. Column (1): source name. Column (2): redshifts from L. Armus et al. (2009). Column (3): luminosity distances from L. Armus et al. (2009). Column (4): infrared luminosities from L. Armus et al. (2009). Column (5): line-of-sight column densities from C. Ricci et al. (2021). Column (6): ratio of IRAS fluxes at 25 μm and 60 μm from D. B. Sanders et al. (2003).
[a] New observations are presented in this work.

(∼ 22″) of these observations is shown as a red circle in Figure 1, overlaid on optical images of the observed galaxies. These targets were observed in the C43-4 and C43-5 ALMA configurations (maximum resolvable scales of 4.″3 and 2.″4, respectively). Table 2 summarizes the observational setup. Atmospheric conditions were reasonable for all observations

Table 2
ALMA Observational Setup and Image Properties

Source	Date of Observations	t_{on} (min)	Configuration	B_{min}/B_{max} (m km^{-1})	Beam Size (arcsec × arcsec,deg)	Beam Size (pc × pc)	Cube rms (mJy beam^{-1})	Continuum rms (mJy beam^{-1})
NGC 4922N	2018 Sep 18	38.32	C43-5	15/1.397	0.38 × 0.24, 16°	188 × 119	0.25	0.06
NGC 7130	2018 Mar 25	5.13	C43-4	14/0.783	0.32 × 0.29, 71°	109 × 99	0.50	0.17
	2018 Sep 9	5.13	C43-4	14/0.783	…	…	…	…
	2018 Sep 24	5.12	C43-5	14/1.397	…	…	…	…
NGC 7674	2018 Sep 19	44.97	C43-5	15/1.397	0.28 × 0.24, 54°	167 × 145	0.19	0.07
NGC 6921	2018 Sep 14	32.18	C43-5	14/1.231	0.39 × 0.27, 12°	115 × 80	0.20	0.09
	2018 Sep 15	32.17	C43-5	14/1.261	…	…	…	…

Note. Column (1): source name. Column (2): date of observations. Column (3): on-source observation time. Column (4): approximate observing configuration. Column (5): minimum and maximum baselines. Column (6): synthesized beam size in arcseconds with position angle in degrees. Column (7): projected synthesized beam size in parsecs. Column (8): rms sensitivity of data cubes, defined as mean 1σ noise level per 33 km s^{-1} channel. Column (9): rms sensitivity of continuum images, defined as mean 1σ noise level. Properties in Columns 7 through 9 are based on combined imaging for all execution blocks for each source.

($T_{sys} \leqslant 100$ K). Two spectral windows were observed for each source, each centered at the redshifted frequencies of HCN (3–2) and HCO^+ (3–2). We adopt the rest frequencies 265.886 GHz and 267.558 GHz for HCN (3–2) and HCO^+ (3–2), respectively. These rest frequencies were obtained from the astronomical spectroscopy database Splatalogue.[15] Spectral windows were set with 1.875 GHz bandwidth and 7.8 MHz spectral resolution.

Data reduction, imaging, and analysis were carried out using the Common Astronomy Software Application (CASA; CASA Team et al. 2022) package version 5.1.1-5. Continuum-subtracted visibilities were created using the automated ALMA imaging pipeline (T. R. Hunter et al. 2023). The NGC 6921 data set, however, was reprocessed with a manually specified frequency range for the continuum fitting and subtraction because the pipeline inadvertently included some line emission in the baseline fit. To improve the signal-to-noise ratio, the data cubes were smoothed to ~33 km s^{-1} channel widths—approximately 4 times that of the observatory-provided pipeline products. Data were imaged with Briggs weighting (robust = 0.5; D. S. Briggs 1995), and resolutions of $\sim 0\farcs3$ were achieved. One millimeter (1 mm) continuum images were also created from the spectral-line-free channels. Table 2 includes a summary of the beam sizes and the rms sensitivities of these new ALMA observations.

2.3. Literature HCN-vib Measurements

From the literature, we obtain HCN-vib surface-brightness measurements and upper limits of five CT-AGNs in U/LIRGs (NGC 1068, IRAS 13120–5453, NGC 5135, NGC 6240N, and NGC 6240S). For NGC 1068, a $\sim 5\sigma$ HCN-vib detection is reported at its western peak at ~2 pc scales (M. Imanishi et al. 2020), but HCN-vib nondetections and upper limits are reported at 10–15 pc scales (M. Imanishi et al. 2016; N. Falstad et al. 2021). In this work, we use the HCN-vib upper limit reported in N. Falstad et al. (2021) at ~15 pc scales, as our fiducial value requires measurements over a region with a radius of at least 5 pc. This also ensures that the HCN-vib measurements were taken over similar angular scales across all sources. For NGC 5135 and IRAS 13120–5453, HCN-vib upper limits are presented in N. Falstad et al. (2021). HCN-vib nondetections are also reported for NGC 6240N and NGC 6240S in Y. Nishimura et al. (2024). For the two nuclei, we calculate 3σ surface-brightness upper limits using the reported HCN (3–2) spectral-line properties and data cube rms, assuming a boxcar profile and a line width equal to the full width at half-maximum (FWHM) of the detected HCN (3–2) line. These HCN-vib measurements and their implications are presented and discussed in Section 4.

3. Results

3.1. 1 mm Continuum

Continuum emission at 1 mm was detected and spatially resolved in all four newly observed CT-AGNs. Their morphology is shown in Figure 2. We assume the peak of the 1 mm continuum to be the AGN position where HCN-vib emission is most likely to be detected. For this reason, we also assign the 1 mm continuum peak to be the position at which we extract the spectral-line profiles (indicated as blue ellipses in Figure 2).

We note that the NGC 7130 continuum is double-peaked with a projected separation of $d_{sep} \approx 250$ pc. Y. Zhao et al. (2016) proposed that the AGN position likely corresponds with the eastern peak due to its alignment with the Very Large Array 8.4 GHz continuum detection. Interestingly, we find that the western peak is brighter in the 1 mm continuum (Figure 2). Though AGN-dominated emission is expected to have a flat millimeter-wave slope ($\alpha_{mm} \approx 0$; T. Kawamuro et al. 2022, where $S \propto \nu^{\alpha}$), the low sensitivity and the limited bandwidth of the observed spectral windows results in spectral index uncertainties as high as $\sim\pm 20$, making it difficult to constrain a precise in-band spectral index. Since further observations are necessary to constrain the AGN position, we present results for both continuum peaks in this paper.

NGC 7674 also has a secondary peak to the northwest ($d_{sep} \approx$ 105 pc). This secondary peak is spatially coincident with the centimeter-wave steep spectral index ($\alpha_{cm} \approx -1$) synchrotron-dominated radio jet identified in Y. Song et al. (2022). The brighter primary peak, in contrast, is spatially coincident with AGN-dominated flat-spectrum ($\alpha_{cm} \approx 0$) radio emission (Y. Song et al. 2022). We therefore assume that the AGN position corresponds to the brighter primary peak for the remainder of this paper.

We measure continuum properties via a two-dimensional Gaussian fit to the continuum map (using the CASA task

[15] https://splatalogue.online/sp_basic.html

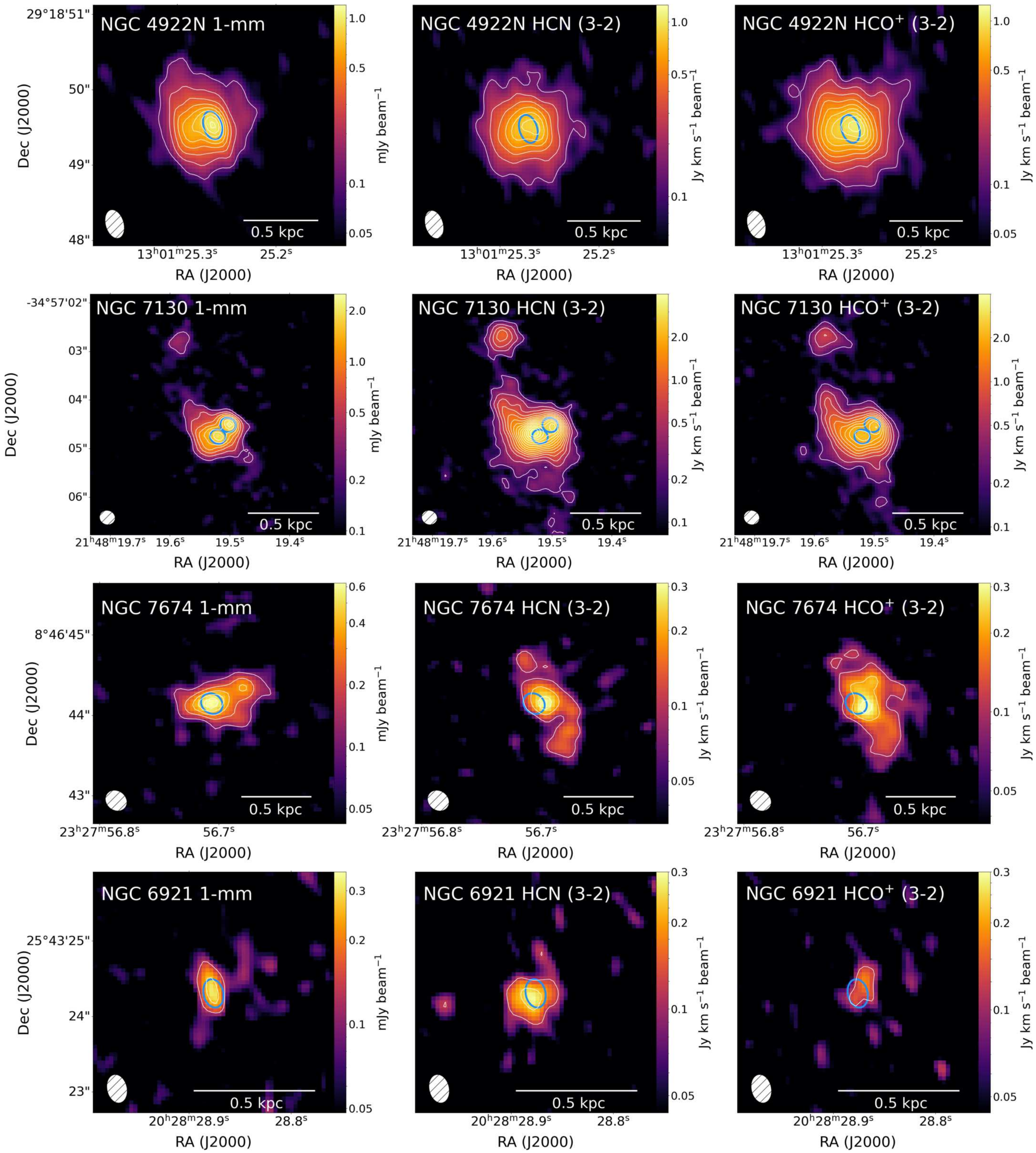

Figure 2. 1 mm continuum and total-intensity (moment 0) maps of HCN (3–2) and HCO^+ (3–2). Each row corresponds to a source (from top to bottom, NGC 4922N, NGC 7130, NGC 7674, and NGC 6921). For each source, the 1 mm continuum image (left) and moment 0 maps for HCN (3–2) (middle) and HCO^+ (3–2) (right) are presented. White contours correspond to 4σ levels (4σ, 8σ, 12σ, …). ALMA-synthesized beam sizes are shown in the bottom left of each map. Blue ellipses correspond to spectral extraction regions for constraining HCN-vib. Note that the images are shown on a logarithmic color scale with the lower limit set to 1σ.

IMFIT) for consistency with N. Falstad et al. (2021). The fit was performed over a region that contained all continuum emission $>3\sigma$. For NGC 7130, two Gaussian components were fitted to account for significant flux contribution from the secondary peak. The peak positions of these two components were fixed to the observed continuum peaks to ensure they were tracing a physical phenomenon. Setting them as free parameters, in contrast, resulted in residual maps with excess

Table 3
Gaussian-fitted Continuum Properties

Source	R.A. of Peak (J2000)	Decl. of Peak (J2000)	Flux Density (mJy)	Continuum Size (mas × mas)	S_{1mm}/Ω (mJy arcsec^{-2})
NGC 4922N	13^{h} 01^{m} 25^{s}.265	+29^{d} 18^{m} 49^{s}.55	4.50 ± 0.23	$738 \pm 33 \times 673 \pm 30$	8.00 ± 0.65
NGC 7130	21^{h} 48^{m} 19^{s}.501*	−34^{d} 57^{m} 04^{s}.50*	2.18 ± 0.35	$376 \pm 41 \times 317 \pm 30$	26.34 ± 3.23
	21^{h} 48^{m} 19^{s}.520[a]	−34^{d} 57^{m} 04^{s}.80*	8.89 ± 0.92	$686 \pm 79 \times 589 \pm 70$	17.62 ± 3.33
NGC 7674	23^{h} 27^{m} 56^{s}.704	+08^{d} 46^{m} 44^{s}.18	2.32 ± 0.17	$762 \pm 52 \times 399 \pm 22$	6.73 ± 0.77
NGC 6921	20^{h} 28^{m} 28^{s}.876	+25^{d} 43^{m} 24^{s}.33	0.48 ± 0.09	$550 \pm 81 \times 287 \pm 25$	2.68 ± 0.68

Note. Column (1): source name. Column (2): J2000 R.A. of the observed 1 mm continuum peak position(s). Column (3): J2000 decl. of the observed 1 mm continuum peak position(s). Column (4): flux density in millijanskys. Column (5): convolved major and minor axes of the 1 mm continuum in milliarcseconds. Column (6): 1 mm continuum surface brightness.

[a] Fixed parameter.

flux at both peaks, indicating a poorer fit. Uncertainty analysis of the two-dimensional Gaussian-fitting method can be found in J. J. Condon (1997). The measured continuum properties are reported in Table 3.

3.2. Dense Gas Tracers

The high dipole moments and high critical densities of HCN (3–2) and HCO^+ (3–2) ($n_{crit} = 10^7\,cm^{-3}$ and $3 \times 10^6\,cm^{-3}$, respectively) make them excellent tracers of high-density gas in galaxies. Here, we study the morphology of the dense gas emission.

We detect HCN (3–2) and HCO^+ (3–2) emission in all of the four observed CT-AGNs. We generate total-intensity (moment 0) maps of the two spectral lines by integrating over all channels with $>3\sigma$ line emission detections using the Python package `Spectral-Cube`. These moment 0 maps are shown in Figure 2. Notably, the morphology of the dense gas emission in NGC 7130 and NGC 7674 appears consistent with the optical spiral arms seen in Figure 1. NGC 4922N and NGC 6921, however, have more centralized emission that is also consistent with the optical images (Figure 1). Furthermore, the continuum and dense gas emission appear to have broadly similar morphologies in all sources, with the exception of NGC 7674.

We also note that NGC 7130 moment 0 maps show double-peaked emission consistent with continuum emission. Intriguingly, the HCN (3–2) emission is brighter in the eastern peak, whereas the western peak is brighter for both HCO^+ (3–2) and the 1 mm continuum. The source of the elevated HCN (3–2) emission around the western peak is briefly explored in Section 3.4.2.

We measure the fluxes of the HCN (3–2) and HCO^+ (3–2) spectral lines at the 1 mm continuum peak by extracting spectra with a beam-sized aperture (blue ellipses in Figure 2). The continuum-subtracted central spectra are presented in Figure 3. We measure the Gaussian FWHM of the line profiles using the Astropy package `specutils`. The observed HCN (3–2) and HCO^+ (3–2) line profiles are relatively narrow and well separated, so the fluxes were extracted over a velocity range with a size twice the Gaussian FWHM. We note that a faint signal is detected at the expected redshifted line center for HCO^+ (3–2) in NGC 6921. Assuming a FWHM equal to the HCN (3–2) line, we measure an integrated flux of 0.11 ± 0.07 Jy km s^{-1} ($\sim 2\sigma$), which we interpret as a marginally significant detection.

We measure spectral-line surface densities Σ_{line} by dividing the line luminosity by the area of the beam-sized aperture (dimensions reported in Table 2). Here, we follow the prescription of P. M. Solomon & P. A. Vanden Bout (2005) and define the line luminosity as

$$\frac{L_{line}}{L_\odot} = \frac{1.04 \times 10^{-3}}{1+z}\left(\frac{S_{line}\Delta v}{\mathrm{Jy\ km\ s^{-1}}}\right)\left(\frac{\nu_{rest}}{\mathrm{GHz}}\right)\left(\frac{D_L}{\mathrm{Mpc}}\right)^2, \quad (1)$$

where L_{line} is the line luminosity, z is the redshift, $S_{line}\Delta v$ is the velocity-integrated flux, ν_{rest} is the rest frequency of the spectral line, and D_L is the luminosity distance. Spectral-line properties and extracted flux measurements are reported in Table 4. For NGC 7130, measurements are reported for both the eastern and western continuum peaks. We find that the line properties are similar across the two peaks.

3.3. Limits on HCN-vib Emission

Bright HCN-vib emission is undetected at the continuum peak of any of the four observed CT-AGNs (Figure 3). We also explore the regions surrounding the continuum peak, but HCN-vib emission is undetected. From the central beam spectra, we place 3σ upper limits on the HCN-vib emission by assuming a boxcar line profile with a width equal to the FWHM of the HCN (3–2) line detection (presented in Table 4). We then apply Equation (1) and divide by the beam area to obtain a surface-brightness upper limit. For example, the NGC 4922N spectrum has a mean 1σ noise level of 0.25 mJy. Over a FWHM of 148 km s^{-1}, this corresponds to a 3σ flux upper limit of $<$0.11 Jy km s^{-1}, or a luminosity upper limit of $<371\ L_\odot$ (Equation (1)). Measured over an aperture area of $\sim$70,283 pc^2 (from the projected elliptical beam size in Table 2), we obtain a 3σ surface-brightness upper limit of $\Sigma_{HCN\text{-}vib} < 0.02\ L_\odot\,pc^{-2}$.

Following this procedure for all targets, we find that the $\Sigma_{HCN\text{-}vib}$ upper limits for the observed CT-AGNs fall below the 1 $L_\odot\,pc^{-2}$ threshold for CONs at $\sim$100 pc scales, indicating that they are not CONs. The measured HCN-vib upper limits are reported in Table 4. Note that we explore the effects of spatial resolution on these measurements in Section 4.1.1.

3.4. Outflows and Nuclear Feedback

Here, we search for molecular outflow signatures in the four observed CT-AGNs to assess the validity of a proposed evolutionary sequence that could link CONs and CT-AGNs.

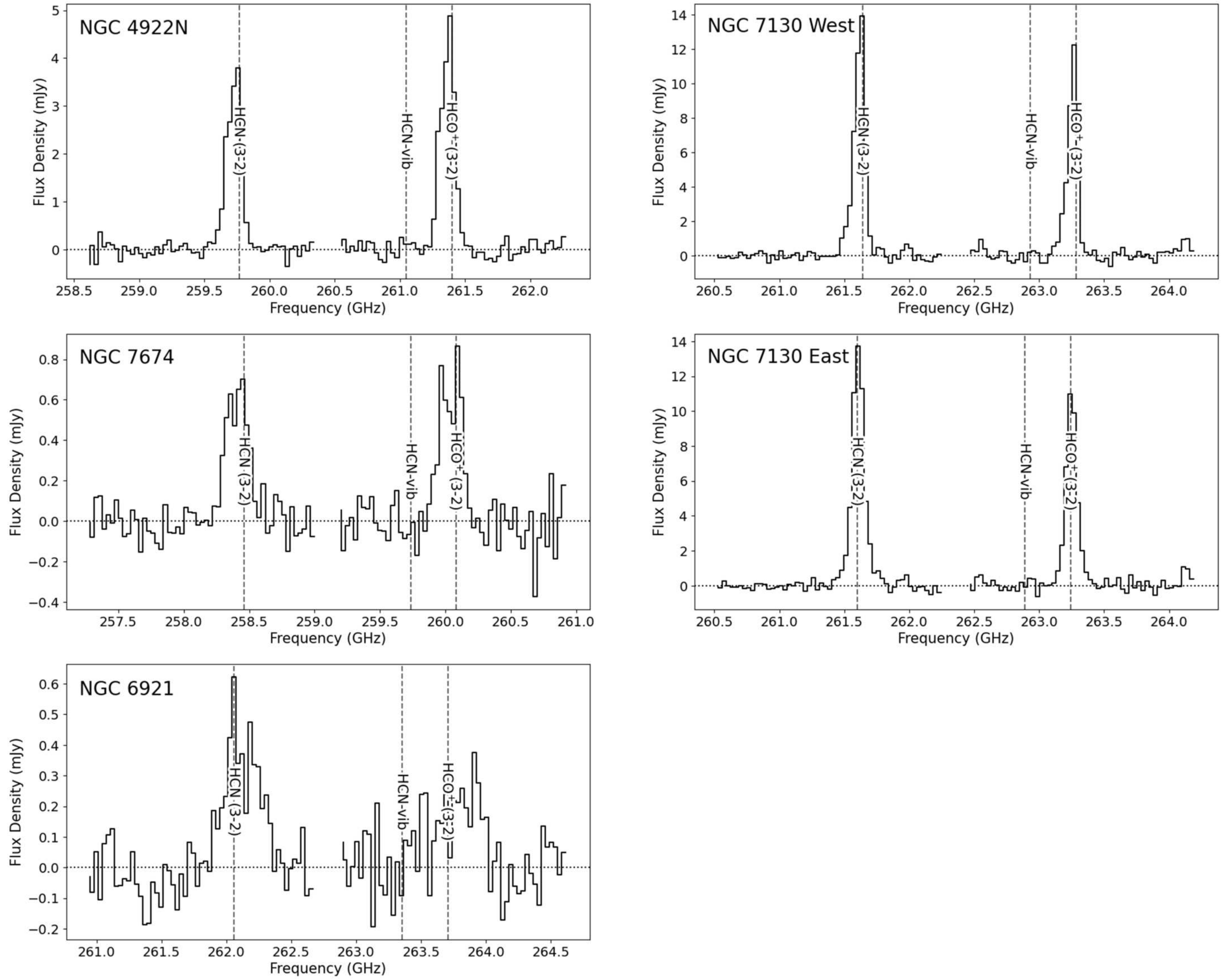

Figure 3. Continuum-subtracted central spectra of the four CT-AGNs with new observations in our sample. The spectra were extracted from the peak of the 1 mm continuum using a beam-sized aperture (cyan ellipses in Figure 2). Redshifted frequencies of HCN (3–2), HCN-vib, and HCO^+ (3–2) are labeled by vertical dashed lines. Systemic velocities were set to match the peak of the HCN (3–2) line profile. The spectral-line frequencies correspond to redshifts $z = 0.02356$ (NGC 4922N), $z = 0.01623$ (NGC 7130 West), $z = 0.01639$ (NGC 7130 East), $z = 0.01460$ (NGC 6921), and $z = 0.02874$ (NGC 7674).

3.4.1. Nuclear Kinematics

We first analyze the nuclear kinematics of the four observed CT-AGNs and search for noncircular motions. Moment 1 (intensity-weighted velocity) and moment 2 (velocity dispersion) maps are presented in Figures 4 and 5, respectively. These images were made using the Python package `Spectral-Cube`, and the extents of the map were determined by masking the data cube to spatial regions where the total intensity (moment 0) is $\geqslant 3\sigma$. The moment 1 maps reveal velocity gradients approximately consistent with rotational motion (Figure 4). Obvious peaks in velocity dispersion, however, are not present in any of the moment 2 maps for the four sources (Figure 5). Note that for NGC 6921, HCO^+ (3–2) emission was omitted from this analysis because the emission was spatially unresolved and had a low signal-to-noise. The HCN (3–2) emission for NGC 6921, however, has the highest velocity dispersion among the four observed CT-AGNs.

Figure 6 shows HCN (3–2) position–velocity (P–V) diagrams taken along the observed major axis. P–V slices were centered on the 1 mm continuum peak (see Figure 2) with a $\sim 2''$ slice length and an approximately beam-sized slice width. For the double-peaked source NGC 7130, we show separate P–V diagrams with slices centered on each peak. Dashed red lines denote the systemic velocity determined from the peak of the HCN (3–2) line in the extracted spectra (see vertical dashed line in Figure 3). The white dashed line shows the location of the 1 mm continuum peak. For the western peak of NGC 7130, the emission feature extending to the left coincides with the position of the source's secondary eastern peak. Due to its low-velocity nature, we conclude that this feature is not indicative of an outflow. In fact, obvious signs of noncircular motion are not seen in any of the P–V diagrams. For all four sources, emission is contained within $\sim 1''$ ($\sim$300–600 pc) offsets from the continuum peak, and relative radio velocities do not exceed $\pm 200\ \mathrm{km\ s^{-1}}$. With limited signs of outflowing molecular gas, the observed nuclear kinematics are instead consistent with the solid-body components of the galaxies' rotation curves.

Table 4
Spectral-line Properties at the 1 mm Continuum Peak

Source	Spectral Line	Line Flux (Jy km s^{-1})	FWHM (km s^{-1})	$\Sigma_{\rm line}$ ($L_\odot$ pc^{-2})
NGC 4922N	HCN (3–2)	0.57 ± 0.04	148 ± 6	0.09 ± 0.01
	HCO$^+$ (3–2)	0.69 ± 0.04	146 ± 6	0.11 ± 0.01
	HCN-vib	<0.11	⋯	<0.02
NGC 7130 West	HCN (3–2)	1.38 ± 0.05	102 ± 3	0.23 ± 0.02
	HCO$^+$ (3–2)	1.15 ± 0.05	95 ± 4	0.19 ± 0.02
	HCN-vib	<0.15	⋯	<0.02
NGC 7130 East	HCN (3–2)	1.81 ± 0.06	110 ± 2	0.28 ± 0.03
	HCO$^+$ (3–2)	1.40 ± 0.06	119 ± 3	0.23 ± 0.02
	HCN-vib	<0.17	⋯	<0.03
NGC 7674	HCN (3–2)	0.15 ± 0.04	226 ± 18	0.03 ± 0.01
	HCO$^+$ (3–2)	0.16 ± 0.04	224 ± 25	0.04 ± 0.01
	HCN-vib	<0.13	⋯	<0.03
NGC 6921	HCN (3–2)	0.16 ± 0.07	357 ± 38	0.02 ± 0.01
	HCO$^+$ (3–2)	0.11 ± 0.07	⋯	0.02 ± 0.01
	HCN-vib	<0.21	⋯	<0.03

Note. Column (1): source name. Column (2): spectral-line name. Column (3): integrated flux at the 1 mm continuum peak in jansky times kilometer per second (Jy km s^{-1}) measured with a beam-sized aperture; uncertainties were estimated using the 1σ rms of the spectrum and an assumed 10% flux uncertainty for ALMA Band 6. Column (4): FWHM of the spectral-line profile; this was measured via a Gaussian fit to the line profile. Column (5): surface brightness of spectral lines in solar luminosity per square parsec ($L_\odot$ pc^{-2}) measured over the beam area; limits are provided at 3σ confidence.

3.4.2. HCN/HCO$^+$ Line Ratio

In a further search for outflow signatures, we investigate spatial regions with elevated HCN/HCO$^+$ line ratios, which can be driven by mechanical heating from outflows (T. Izumi et al. 2015; T. Izumi et al. 2016). Thus, spectral extractions from HCN-enhanced spatial regions could reveal outflow signatures via extended line wings. The left-hand panel of Figure 7 shows the spatially resolved $L_{\rm HCN(3-2)}/L_{\rm HCO^+(3\text{-}2)}$ ratios of NGC 4922N, NGC 7130, and NGC 7674. NGC 6921 is again omitted from this analysis because the HCO$^+$ (3–2) emission was not spatially resolved and had a low signal-to-noise. We created this figure by taking the ratio of the HCN (3–2) and HCO$^+$ (3–2) total-intensity maps after masking out the regions where HCN (3–2) is not detected at $\geqslant 3\sigma$.

Beam-sized ellipses on the left-hand panel denote spatial regions from which HCN (3–2) spectra were extracted. These apertures are both numbered and colored to match their corresponding spectra, which are displayed on the right-hand panel. For NGC 4922N, significant elevations in the line ratio are not observed. NGC 7130 and NGC 7674, however, reveal notable elevations in relative HCN (3–2) brightness. Though spectral extractions at these elevated spatial regions show asymmetries and line wings in the line profiles (notably, panel 2 for NGC 4922N and panel 3 for NGC 7130), the features are contained within $\sim\pm 200$ km s^{-1} of the systemic velocity, and obvious indicators of high-velocity molecular outflows are not present. We conclude that while low-velocity ($\lesssim 200$ km s^{-1}) noncircular motions may be present, fast outflows are not detected in regions with elevated HCN/HCO$^+$ ratios, and further investigation is necessary to determine the driver of the enhanced line ratio.

4. The Connection between CT-AGNs and CONs in Local U/LIRGs

4.1. Are CT-AGNs Also CONs?

Here, we combine our new continuum and HCN-vib measurements of four CT-AGNs with the literature measurements of five additional CT-AGNs. We can now compare the properties of the complete CT-AGN sample with those of CONs. N. Falstad et al. (2021) found that CONs have both high HCN-vib surface brightnesses ($\Sigma_{\rm HCN\text{-}vib} > 1\ L_\odot$ pc^{-2}) and 1 mm continuum surface brightnesses ($S_{\rm 1mm}/\Omega \gtrsim$ 1000 mJy arcsec^{-2}), with both properties serving as tracers of high-column-density regions. In Figure 8, we compare our complete sample of nine CT-AGNs to other local U/LIRGs (including CONs) by plotting $\Sigma_{\rm HCN\text{-}vib}$ with respect to $S_{\rm 1mm}/\Omega$ where measurements were available in the literature. All plotted sources were observed at $\sim$0$''$.2–0$''$.8 angular resolutions ($\lesssim$100 pc scales; N. Falstad et al. 2019, 2021; Y. Nishimura et al. 2024; this work). Note that we plot measurements for both continuum peaks of NGC 7130 since the exact AGN position is unknown, resulting in 10 plotted values for our complete sample of nine CT-AGNs. We find that the CT-AGNs (shown in blue) have lower HCN-vib surface brightnesses and lower 1 mm continuum surface brightnesses than CONs (shown in red).

In our comparison, we account for a methodological difference: N. Falstad et al. (2021) measured $\Sigma_{\rm HCN\text{-}vib}$ across the continuum area defined by a Gaussian fit, whereas we report HCN-vib upper limits measured specifically with a beam-sized aperture at the continuum peak in Table 4. While we elect to report upper limits measured from the region where HCN-vib emission is most likely, we plot remeasured $\Sigma_{\rm HCN\text{-}vib}$ upper limits in Figure 8. These values were calculated using spectra extracted with a continuum-sized aperture (dimensions reported in Table 3). This ensures that the plotted $\Sigma_{\rm HCN\text{-}vib}$ values and $S_{\rm 1mm}/\Omega$ values were measured over the same area. The remeasured values are listed in Table 5. The plotted HCN-vib measurements of CT-AGNs in local U/LIRGs are listed in Table 5.

Figure 8 reveals that the HCN-vib surface brightnesses and 1 mm continuum surface brightnesses of CT-AGNs do not overlap with those of the CONs. In fact, all NuSTAR hard-X-ray-confirmed CT-AGNs have $\Sigma_{\rm HCN\text{-}vib} < 1\ L_\odot$ pc^{-2} (S. Martín et al. 2016; N. Falstad et al. 2019, 2021; Y. Nishimura et al. 2024), translating to a CON detection rate of 0^{+17}_{-0}% in CT-AGNs. Here, the 1σ confidence intervals were estimated using the beta-distribution quantile technique, which assigns a probability density function to an assumed binomial population. This method is outlined in E. Cameron (2011).

The observed CT-AGNs also lack significant self-absorption features in the HCO$^+$ (3–2) and HCN (3–2) line profiles (Figures 3 and 7). CONs, on the other hand, have double-peaked spectral lines (e.g., IC 860; S. Aalto et al. 2019) that indicate the absorption of photons by an enshrouding layer of cooler gas (S. Aalto et al. 2015a). With the exception of NGC 7674, the observed spectral lines are not double-peaked (see Figures 3 and 7), suggesting that the line-of-sight column densities of these CT-AGNs may be smaller than those of typical CONs.

CT-AGNs and CONs may also differ in their infrared spectral energy distributions (SEDs), but we cannot fully explore this property due to a sample selection bias. N. Falstad

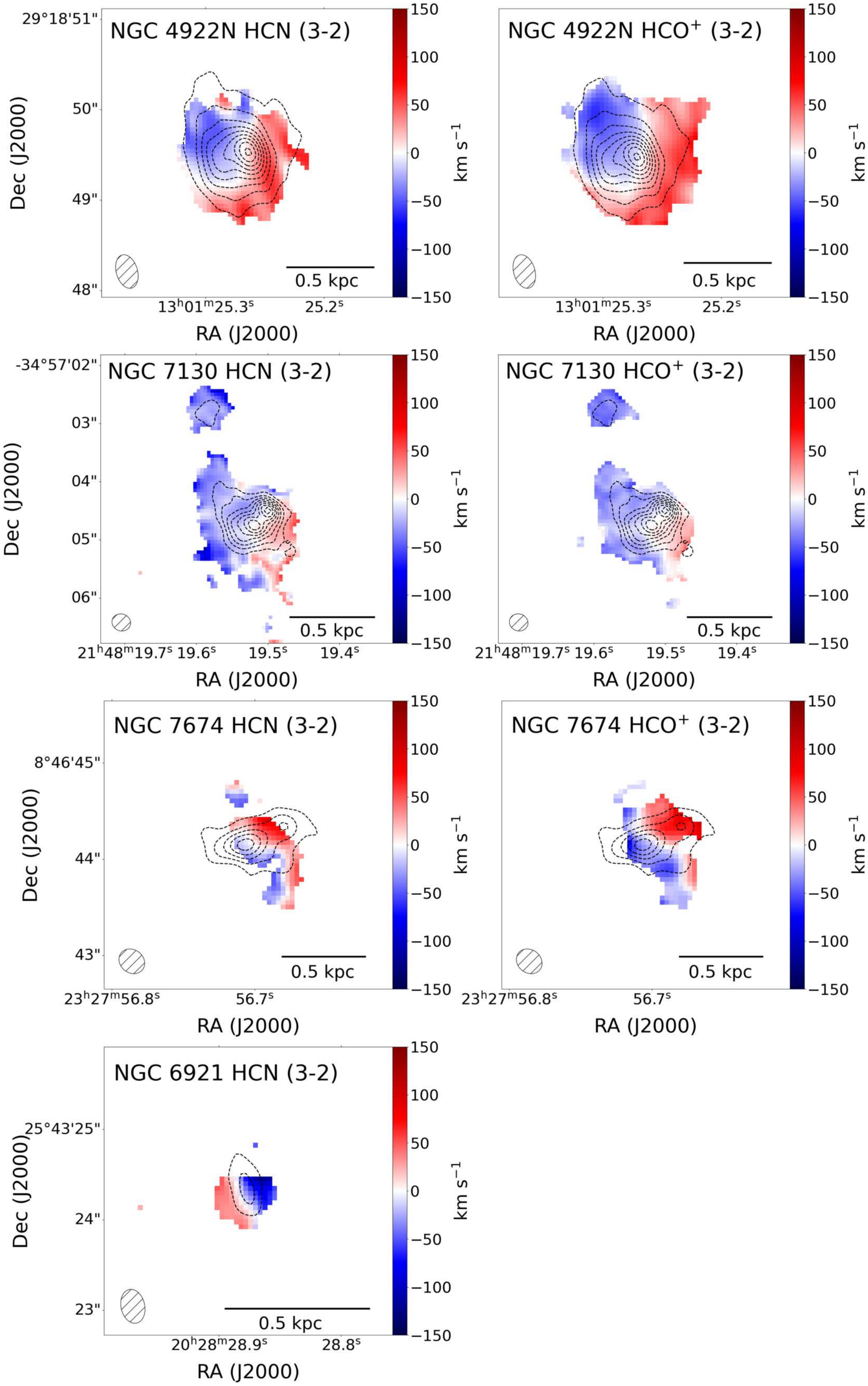

Figure 4. Intensity-weighted velocity (moment 1) maps of HCN (3–2) (left) and HCO^+ (3–2) (right). Each row corresponds to a source (from top to bottom, NGC 4922N, NGC 7130, NGC 7674, and NGC 6921). Moment 1 map extents were created by masking the data cube to where the total intensity (moment 0) $\geqslant 4\sigma$. 1 mm continuum contours (4σ levels) are overlaid as black dashed lines. Note that NGC 6921 HCO^+ (3–2) emission is omitted because the emission features were faint and unresolved.

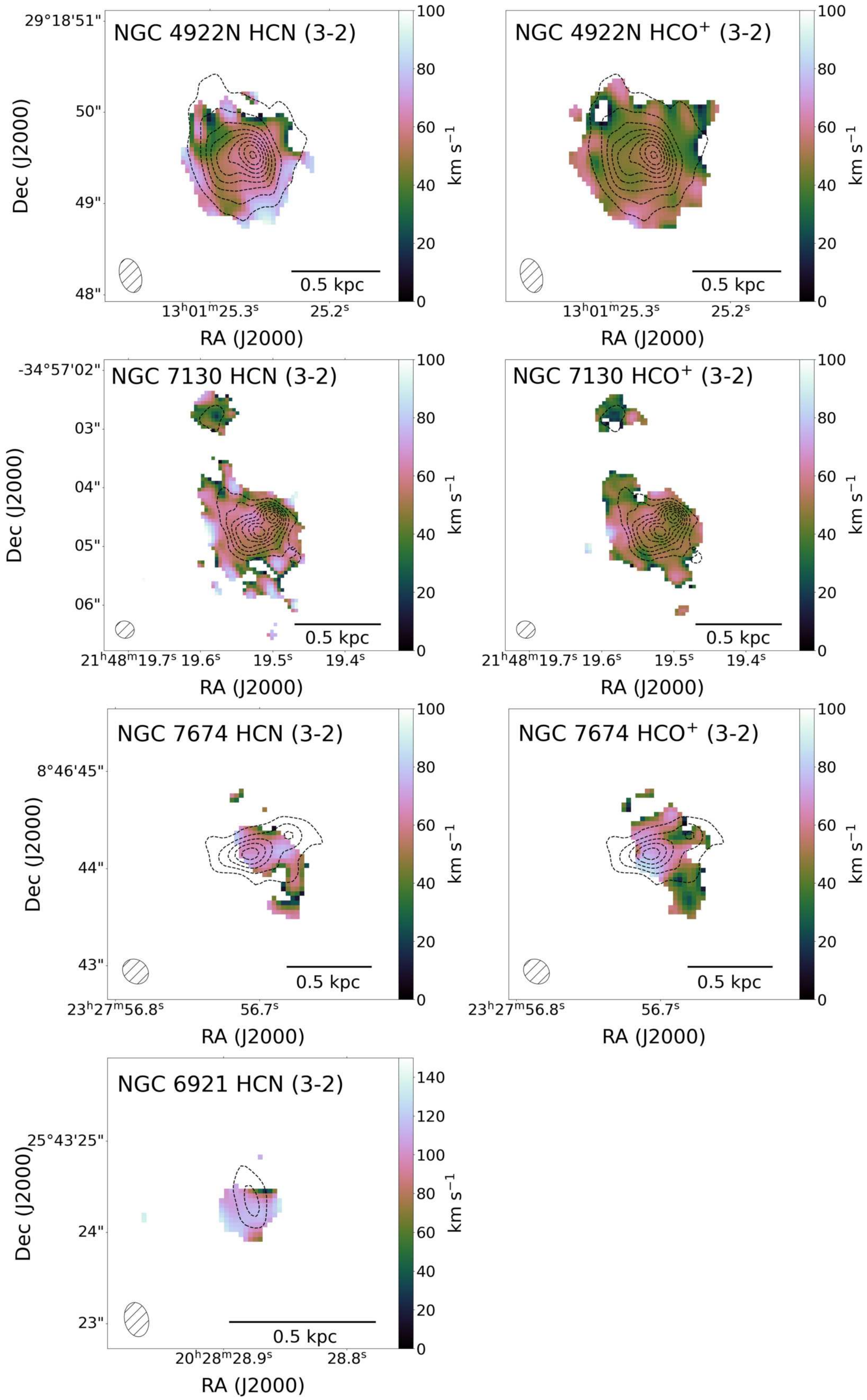

Figure 5. Velocity dispersion (moment 2) maps of HCN (3–2) (left) and HCO$^+$ (3–2) (right). Each row corresponds to a source (from top to bottom, NGC 4922N, NGC 7130, NGC 7674, and NGC 6921). Moment 2 map extents were created by masking the data cube to where the total intensity (moment 0) $\geqslant 4\sigma$. 1 mm continuum contours (4σ levels) are overlaid as black dashed lines. Note that the NGC 6921 HCN (3–2) emission is shown with a wider dynamic range on the color scale due to its higher velocity dispersions. NGC 6921 HCO+ (3–2) emission is omitted because the emission features were faint and unresolved.

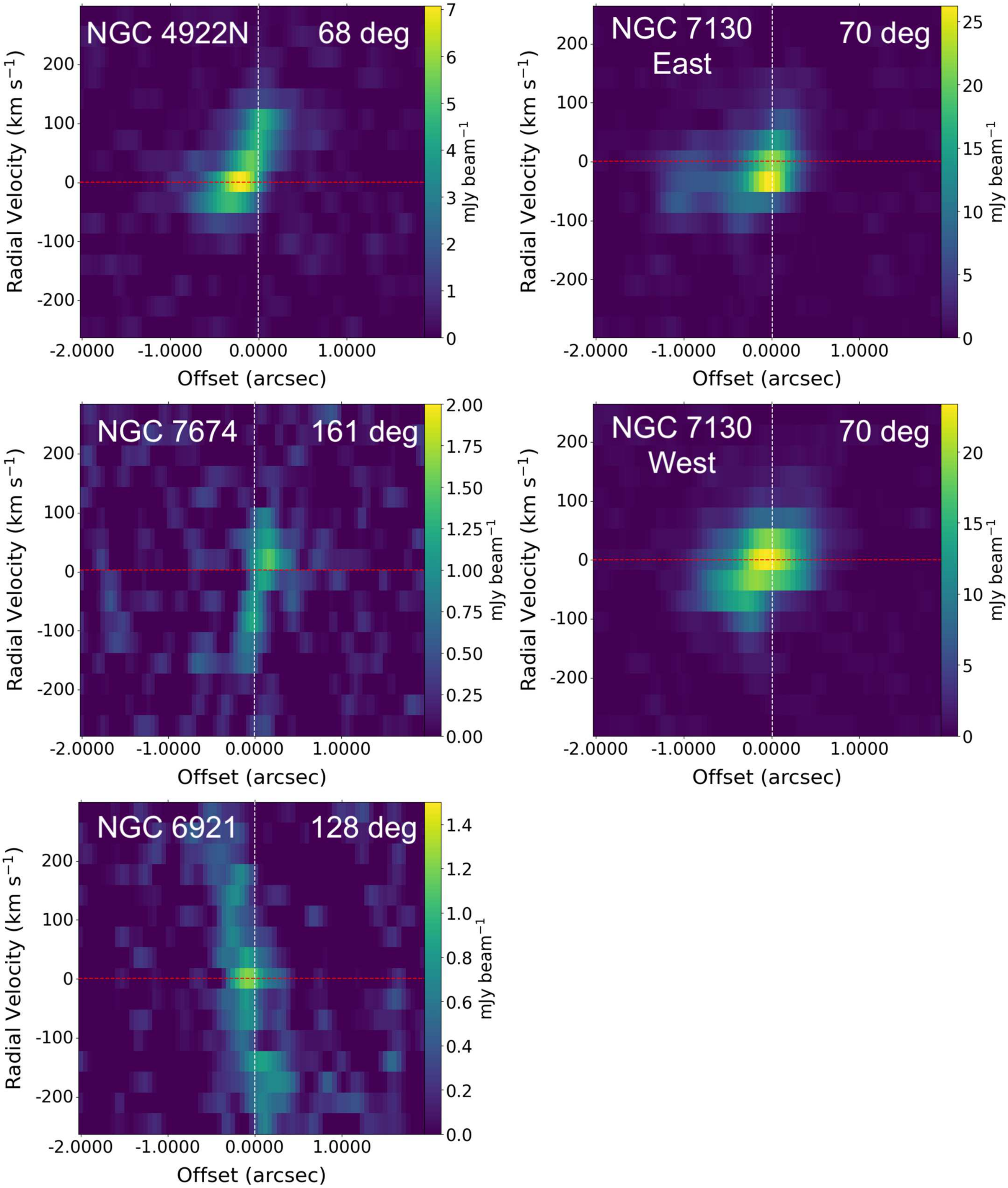

Figure 6. Position–velocity (P–V) diagrams of the observed CT-AGNs. P–V diagrams were created from a $\sim 2''$-long beamwidth slice along the observed major axis of the velocity field. The position angles of the slices are shown in the top right of each plot. Red lines mark 0 km s^{-1}, corresponding to the systemic velocity determined from the peak of the HCN (3–2) position. Vertical dashed white lines mark the position of the 1 mm continuum peak.

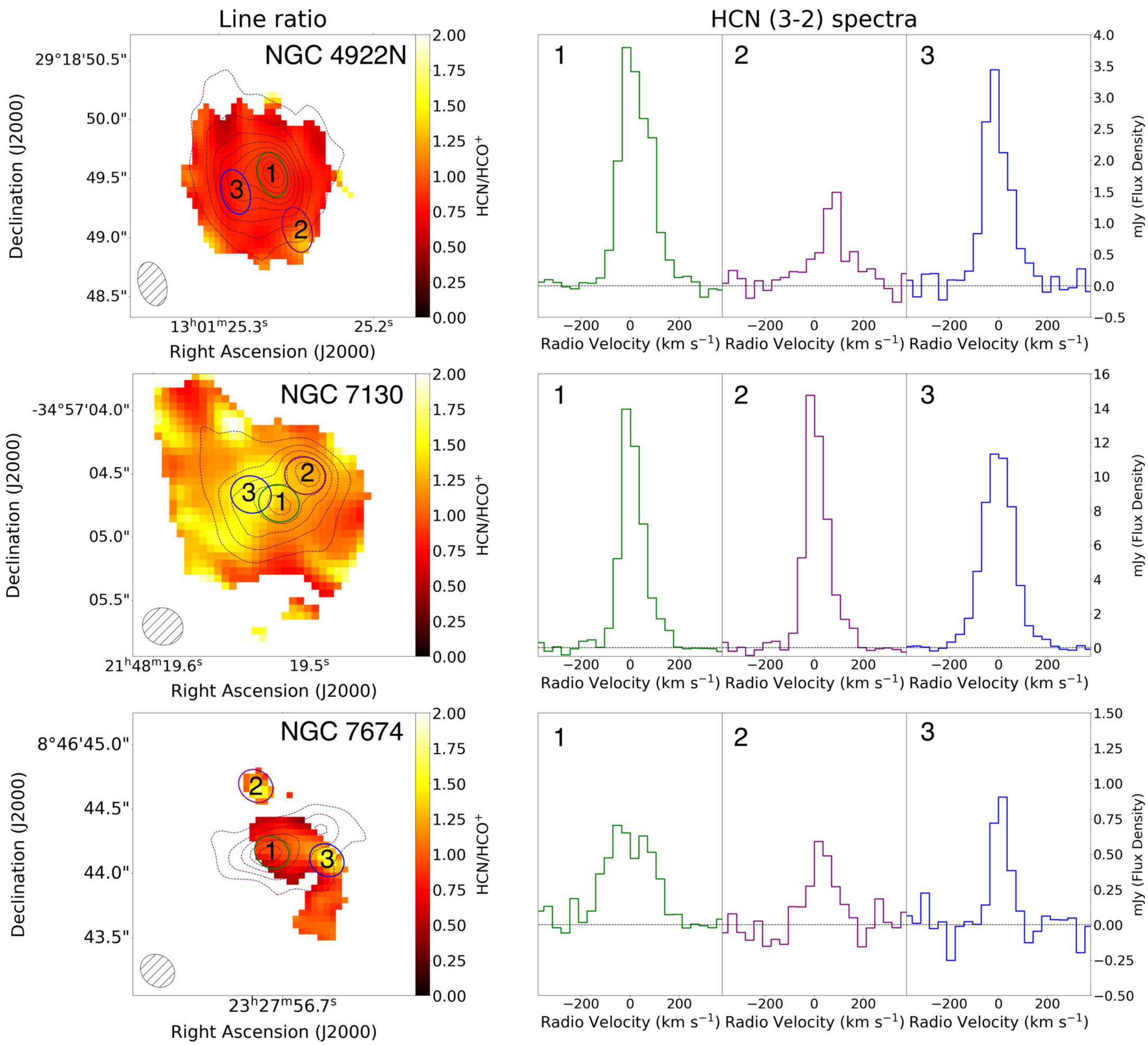

Figure 7. Left: spatially resolved HCN (3–2)/HCO$^+$ (3–2) ratio maps of observed CT-AGNs. Right: continuum-subtracted HCN (3–2) spectra extracted from beam-sized apertures. Beam-sized ellipses on the HCN (3–2)/HCO$^+$ (3–2) ratio map indicate spectral extraction regions. Dashed contours indicate 1 mm continuum emission. Spectra are numbered and shown in the same color as their corresponding ellipses.

et al. (2021) found that CONs have low IRAS flux ratios at 25 μm and 60 μm (f_{25}/f_{60}), but the surveyed sample was biased toward sources with cooler infrared SEDs. Our sample of hard-X-ray-confirmed CT-AGNs includes both warm ($f_{25}/f_{60} > 0.2$) and cool ($f_{25}/f_{60} < 0.2$) sources (see Table 1), revealing a different f_{25}/f_{60} distribution than the CONs detected by N. Falstad et al. (2021). While this could indicate a significant difference in the properties of CT-AGNs and CONs, we cannot precisely compare their f_{25}/f_{60} distributions until an unbiased search for warm CONs is conducted.

4.1.1. Impact of Spatial Resolution

The $\Sigma_{\text{HCN-vib}}$ upper limits in Table 5 demonstrate that CT-AGNs in U/LIRGs generally do not have HCN-vib detections at ~100 pc scales. While this could indicate that the CT-AGNs have a weaker mid-infrared radiation field than CONs (and thus cannot excite HCN molecules into vibrationally excited states), the inferred $\Sigma_{\text{HCN-vib}}$ upper limits could be affected by insufficient spatial resolution. We consider here that CT-AGNs in U/LIRGs may have smaller HCN-vib emission regions than the spatial scales probed in this work. This is motivated by previous studies of the CT-AGN NGC 1068 that detected high-surface-brightness HCN-vib emission at ~2 pc spatial resolution ($\Sigma_{\text{HCN-vib}} = 1.6\ L_\odot\ \text{pc}^{-2}$; M. Imanishi et al. 2016) but a nondetection at ~15 pc scales ($\Sigma_{\text{HCN-vib}} < 0.13\ L_\odot\ \text{pc}^{-2}$; N. Falstad et al. 2021).

We evaluate the effects of spatial resolution on $\Sigma_{\text{HCN-vib}}$ by approximating the HCN-vib emission region as a single point source for each CT-AGN. We can then estimate the aperture

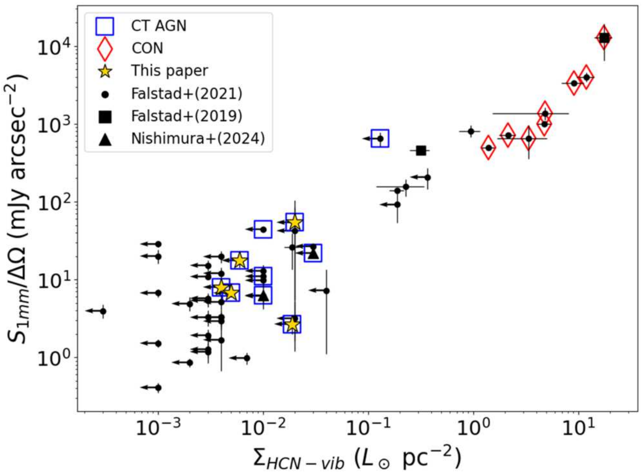

Figure 8. 1 mm continuum surface brightness as a function of HCN-vib surface brightness. Arrows indicate upper limits. CONs and CT-AGNs are marked in red and blue, respectively. Both axes are on a logarithmic scale. This figure was adapted from Figure 10 in N. Falstad et al. (2021). From their low HCN-vib surface brightnesses, we find that CT-AGNs are lacking CON-like infrared cores.

Table 5
Continuum-area HCN-vib Measurements of CT-AGNs in U/LIRGs

Source	$\Sigma_{\text{HCN-vib}}$ ($L_\odot$ pc^{-2})	$L_{\text{HCN-vib}}/L_{\text{IR}}$ (10^{-8})	References
NGC 1068	<0.13	<0.004	N. Falstad et al. (2021)
NGC 4922N	<0.004	<0.153	This work
13120–5453	<0.01	<0.108	N. Falstad et al. (2021)
NGC 5135	<0.01	<0.085	N. Falstad et al. (2021)
NGC 6240N	<0.01	<0.128	Y. Nishimura et al. (2024)
NGC 6240S	<0.03	<0.238	Y. Nishimura et al. (2024)
NGC 6921	<0.03	<0.249	This work
NGC 7130 E	<0.02	<0.082	This work
NGC 7130 W	<0.006	<0.085	This work
NGC 7674	<0.005	<0.120	This work

Note. Column (1): source name. Column (2): HCN-vib surface brightnesses and upper limits in solar luminosity per square parsec ($L_\odot$ pc^{-2}); limits are provided at 3σ confidence. Column (3): HCN-vib luminosity-to-infrared luminosity ratio; limits are provided at 3σ confidence. Column (4): literature sources from which HCN-vib measurements were obtained.

size necessary to obtain an HCN-vib surface-brightness measurement that is consistent with the CON criterion ($\Sigma_{\text{HCN-vib}} \geqslant 1\ L_\odot$ pc^{-2}). Note that this approximation assumes that the line luminosity remains constant, and only the radius of the aperture is adjusted (i.e., the emission region size). If we assume a HCN-vib line luminosity equal to the 3σ upper limit (see Table 5), then the radius upper limit ranges from $r <$ 4–26 pc and a median of $r < 16$ pc to have a sufficiently high $\Sigma_{\text{HCN-vib}}$. A 1σ line luminosity requires an even more compact core, with $r <$ 2–15 pc and a median upper limit of $r < 10$ pc. We emphasize that our empirical fiducial value of $\Sigma_{\text{HCN-vib}} > 1\ L_\odot$ pc^{-2} for CONs was selected for measurements taken over a region with $r > 5$ pc (N. Falstad et al. 2021), and smaller radii are inconsistent with the observed properties of CONs.

We also consider the fiducial value $L_{\text{HCN-vib}}/L_{\text{IR}} > 10^{-8}$, which was used by early studies of CONs (e.g., S. Aalto et al. 2015a; N. Falstad et al. 2019). Though this luminosity ratio is a less robust metric because the infrared emission can have contributions from nonnuclear regions of the galaxy, it nevertheless offers a criterion that is less influenced by the systematic effects of spatial resolution. In Table 5, we report $L_{\text{HCN-vib}}/L_{\text{IR}}$ ratio measurements of the CT-AGNs studied in this work. We find that the CT-AGNs are not CONs with respect to both the $\Sigma_{\text{HCN-vib}}$ criterion and the $L_{\text{HCN-vib}}/L_{\text{IR}}$ criterion.

Though we cannot eliminate the possibility that our sample of CT-AGNs has parsec-scale CON-like HCN-vib emission regions, the nondetections of CONs across both fiducial values combined with the clear divergence in the HCN-vib properties at ∼100 pc scales demonstrate that CONs and CT-AGNs are distinct phenomena in U/LIRGs. We therefore conclude that the limited spatial resolution does not significantly affect the broader conclusion of this work.

4.2. Evolutionary Link: Do CT-AGNs Evolve from CONs?

Although the properties of CT-AGNs deviate from those of CONs at ∼100 pc scales, their gas kinematic features could provide insight into their potential evolutionary link to CONs. CONs host collimated molecular outflows with maximum velocities ranging from 300 km s^{-1} (ESO 320-G030; M. Pereira-Santaella et al. 2016) to 840 km s^{-1} (Arp 220W; L. Barcos-Muñoz et al. 2018). Here, we explore the proposed feedback-driven evolutionary sequence in which CT-AGNs would have faster and more evolved molecular outflows than the collimated features found in CONs (E. González-Alfonso et al. 2017; N. Falstad et al. 2019, 2021).

Based on the line luminosities of known HCN outflows in CONs, we confirm that our sensitivities are sufficient to detect similar outflows in our observed CT sample, if they are present. Specifically, the HCN (3–2) outflow in ESO 320-G030 (M. D. Gorski et al. 2024) would have been detected at a 8–28σ level. Likewise, the HCN (1–0) outflow in Arp 220W (L. Barcos-Muñoz et al. 2018) would have been detected at a 3–11σ level. The latter calculation assumes an HCN (3–2) to HCN (1–0) luminosity ratio of 0.5 (S. Aalto et al. 2015b; M. D. Gorski et al. 2024).

Despite this potential for outflow detection, we find no signs of high-velocity (>200 km s^{-1}) noncircular motion in the HCN (3–2) emission of the four observed CT-AGNs. Such nondetections are inconsistent with the proposed evolutionary sequence. Examining the literature on our combined sample of nine CT-AGNs, however, we find that a significant fraction of them do host fast molecular outflows. Specifically, high-velocity (>500 km s^{-1}) CO outflows have been detected in NGC 6240 (a merger system containing two CT-AGNs, NGC 6240N and NGC 6240S; C. Feruglio et al. 2013; E. Treister et al. 2020). Dense molecular outflows have also been observed in NGC 1068 and IRAS 13120–5453 with velocities of ∼300 km s^{-1} (S. García-Burillo et al. 2014; G. C. Privon et al. 2017; D. Lutz et al. 2020). Of the nine hard-X-ray-confirmed CT-AGNs, we find that at least 44% (4/9) host molecular outflows.[16]

According to the proposed sequence, these molecular outflows may have evolved from the collimated outflows of

[16] We acknowledge that it is unclear whether all of these molecular outflows are powered by an AGN. Specifically, NGC 6240 hosts a multicomponent outflow with both a likely starburst-driven component and a likely AGN-driven component (F. Müller-Sánchez et al. 2018). This ambiguity makes it difficult to assess whether the outflow properties of NGC 6240 agree with the proposed evolutionary link between CONs and CT-AGNs.

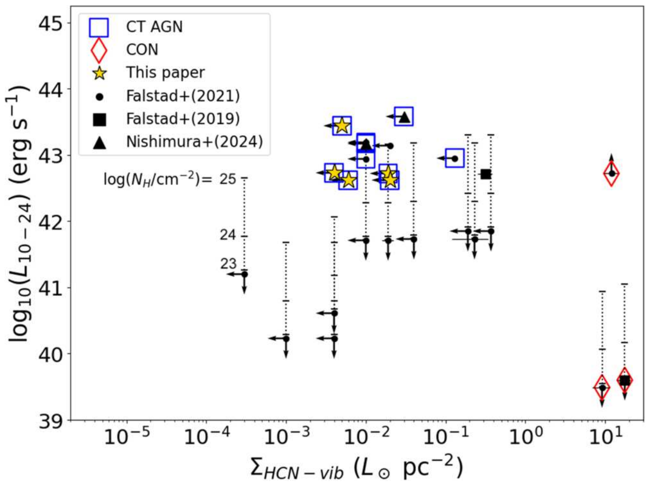

Figure 9. Extinction-corrected hard X-ray luminosity vs. HCN-vib surface brightness of CT-AGNs and CONs. CT-AGNs are marked in blue, and CONs in red. Arrows indicate upper limits. Dotted lines show N_H corrections for X-ray luminosity upper limits, with the upper limits shifting to the subsequent tick for every order-of-magnitude increase in line-of-sight column density. The limited number of hard X-ray detections of CONs (shown in red) suggests that if CONs host CT-AGNs, they are likely undetectable at hard X-ray wavelengths.

CONs. We estimate the ages of the outflows to test this theory. We find that the collimated outflows have short predicted dynamical times (∼0.2 Myr; M. Pereira-Santaella et al. 2016; L. Barcos-Muñoz et al. 2018; N. Falstad et al. 2018; D. Lutz et al. 2020), whereas the molecular outflows in CT-AGNs have comparatively older outflow ages ($\gtrsim$1 Myr; C. Feruglio et al. 2013; S. García-Burillo et al. 2014; D. Lutz et al. 2020; E. Treister et al. 2020). The presence of these older, well-developed molecular outflows coupled with weak HCN-vib emission makes these CT-AGNs qualitatively consistent with the proposed sequence of evolution.

Detections of large-scale ionized outflows in CT-AGNs may also be consistent with the proposed sequence, considering that the gas in a previous CON-like molecular outflow may have been ionized by the central source. The larger physical scales of ionized outflows often indicate that they are older than the assumed duration of the active feedback phase (∼1 Myr), possibly associating them with a previous epoch of CON activity. For example, ionized outflows with estimated expansion times of 3−11 Myr have been observed in some CT-AGNs in U/LIRGs (e.g., NGC 7130 and NGC 6240; F. Müller-Sánchez et al. 2018; S. Comerón et al. 2021).

Given that some CT-AGNs host well-developed outflows while others do not, it is possible that there are multiple evolutionary paths for CT-AGNs, with some sources evolving from CONs as previously theorized and others having never entered a CON phase. We find evidence of this theory in the fact that the estimated lifetime of the CON phase is significantly shorter (∼1 Myr; S. Aalto et al. 2019) compared to that of the CT-AGN phase (∼100 Myr). The ratio of these estimated timescales implies that even if all CONs evolve into CT-AGNs, they would only account for 1% of the CT-AGN population. This further suggests that only a small subset of CT-AGNs is likely related to CONs.

In an idealized scenario, the presence of outflows could be used to distinguish between CT-AGNs that evolved from CONs and those that did not. Unfortunately, CT-AGNs without active molecular outflows could still have evolved from CONs if the outflow activity is episodic. That is, the outflow may have become inactive after entering the CT-AGN phase, resulting in a nondetection. This model is supported by ample theoretical and observational evidence of episodic outflow activity in local U/LIRGs, which then makes it reasonable to infer similar mechanisms in CONs and CT-AGNs. For example, fast blow-out phases are predicted by the radiative feedback model (∼1 Myr; P. F. Hopkins et al. 2008; C. Ricci et al. 2017c; C. Ricci et al. 2022; N. Yutani et al. 2022), implying short-lived active feedback mechanisms. Outflow “fossils” from previous epochs of outflow activity have also been detected in local U/LIRGs (e.g., A. W. Janssen et al. 2016; R. Herrera-Camus et al. 2020; D. Lutz et al. 2020). A complete search for these outflow relics in CONs and CT-AGNs, however, has not been conducted and will be necessary to fully evaluate the model.

The possibility of episodic outflow activity as well as multiple evolutionary paths complicates current and future studies of CON evolution. The proposed sequence, however, necessitates the existence of nuclei that are in the process of transitioning out of a CON phase and into a CT-AGN phase. Direct detection of these intermediate-stage sources as well as the characterization of their outflow properties and their HCN-vib emission will inform and constrain the evolutionary model. The future directions and observational limitations of this research are discussed in Section 4.3 below.

4.3. Sample Selection Bias: Heavily CT-AGN

Here, we consider the effects of a potential sample selection bias on the low measured rate of the occurrence of CONs in U/LIRGs that host CT-AGNs.

Examining the intrinsic properties of the CT-AGNs in our sample, we find limited spread in their extinction-corrected hard X-ray luminosities. This is consistent with the findings of C. Ricci et al. (2021), who reported that obscured AGNs tend to have higher intrinsic X-ray luminosities than unobscured AGNs. Figure 9 is a plot of the 10−24 keV intrinsic X-ray luminosities from the literature (S. H. Teng et al. 2015; S. Puccetti et al. 2016; P. Gandhi et al. 2017; C. Ricci et al. 2017b, 2017d; S. Oda et al. 2018; S. Yamada et al. 2020; C. Ricci et al. 2021) with respect to the HCN-vib surface brightnesses of local U/LIRGsU/LIRGs (this work; N. Falstad et al. 2019, 2021; Y. Nishimura et al. 2024). Arrows indicate upper limits for HCN-vib surface brightness and X-ray luminosity. Dotted lines are NH corrections for undetected but possibly obscured sources. Note that the low number of data points from N. Falstad et al. (2021) is due to the limited number of published hard X-ray measurements for the sample.

Though hard X-ray studies offer a reliable and direct means of identifying AGNs, X-ray studies of CONs have been unable to detect AGNs (as demonstrated by the CON nondetections/upper limits in Figure 9). Despite these AGN nondetections in the X-ray, a starburst scenario is also uncertain as it would require O-star-dominated IMFs at 10−100 pc scales (S. Aalto et al. 2019). An alternative interpretation, one that is consistent with our proposed evolutionary model, is that CONs host reflection-dominated AGNs with large gas columns and covering factors that significantly reduce X-ray detections. In fact, C. Ricci et al. (2017a) finds that the observed rate of “heavily CT” AGNs ($N_H > 10^{25}$ cm^{-2}) in the local Universe is significantly lower than the intrinsic rate determined from the inferred N_H distribution. Models further suggest that a high fraction of AGNs are X-ray obscured (M. A. Worsley et al. 2005; C. M. Carroll et al. 2023; G. Mazzolari et al. 2024). Indeed, with the exception of NGC 4922N, there is an absence of sources with line-of-sight column densities $N_H > 10^{25}$ cm^{-2} in our sample. Thus, our study does not eliminate the possibility that CONs are an extreme subset of CT-AGNs ($N_H > 10^{25}$ cm^{-2}) that are nondetectable at X-ray wavelengths due to attenuation.

If CONs are driven by heavily CT AGNs, a source of interest would be Arp 220W, a known CON (S. Aalto et al. 2015a; S. Martín et al. 2016; K. Sakamoto et al. 2021) with an estimated column density as high as $N_H \approx 10^{26}$ cm^{-2} (N. Scoville et al. 2017). NuSTAR observations detect X-ray emission that is consistent with only a starburst, but due to its high column density, a deeply buried AGN may be present in Arp 220W (S. H. Teng et al. 2015). In fact, recent studies have uncovered evidence of possibly AGN-driven outflows (E. Varenius et al. 2016; L. Barcos-Muñoz et al. 2018). The AGN nature of the CON Arp 220W has been fiercely debated due to this mixed evidence, and there is increased urgency to identify new techniques for detecting AGNs in heavily obscured environments.

A promising solution is the recently identified millimeter–X-ray relation (T. Kawamuro et al. 2022; C. Ricci et al. 2023), which has the potential to confirm (or dispute) the presence of an AGN in Arp 220W and other heavily obscured nuclei. The tight correlation between AGN X-ray luminosity and millimeter-wave luminosity (T. Kawamuro et al. 2022; C. Ricci et al. 2023) suggests that flat-spectrum ($\alpha_{mm} \approx 0$) millimeter-wave emission could be used to derive the intrinsic X-ray luminosities of heavily obscured AGNs (and subsequently their bolometric luminosities). Since millimeter waves are almost unaffected by dust extinction until $N_H \sim 10^{26}$ cm^{-2}, millimeter-wave observations may prove to be essential in the search for these "missing" heavily CT AGNs.

We also note that there is a need to search for CONs in CT-AGNs outside of the U/LIRGs in the GOALS sample (e.g., CT-AGNs in post-starburst galaxies), which would provide a statistic on the prevalence of CONs in a more complete sample of CT-AGNs. The apparent strong infrared luminosity dependence of the CON phenomena (N. Falstad et al. 2021), however, makes it unlikely that such a search would be fruitful.

5. Conclusion

We study the prevalence of CONs in CT-AGNs in local U/LIRGs by analyzing ALMA Band 6 HCN-vib observations of four local U/LIRGs hosting a CT-AGN, combined with five additional sources with HCN-vib literature data. We study this combined sample of nine CT-AGNs with HCN-vib measurements to analyze the potential connection between CT-AGNs and CONs in local U/LIRGs. Our results are as follows.

1. Using the fiducial value of $\Sigma_{\text{HCN-vib}} \geqslant 1\, L_\odot$ pc^{-2}, we find a CON detection rate of 0^{+17}_{-0}% in hard-X-ray-detected CT-AGNs in local U/LIRGs (see Figure 8). These CT-AGNs also have significantly fainter 1 mm continuum surface brightnesses compared to CONs. This reveals that X-ray-confirmed CT-AGNs do not host CONs.
2. While all known CONs have shown evidence of molecular outflows (N. Falstad et al. 2021), we do not find any evidence of significant high-velocity noncircular motion in the dense gas emission of four observed CT-AGNs (Figures 6 and 7). We note, however, that fast molecular outflows have been reported in the literature for 4/9 (44%) of the CT-AGNs in our sample. The fact that some CT-AGNs in U/LIRGs host molecular outflows while others have nondetections suggests that there may be multiple evolutionary paths for CT-AGNs (with some evolving from a prior CON phase and others not). Alternatively, this could be indicative of a relatively short outflow duty cycle compared to the timescale of the CT phase of AGN evolution.

Acknowledgments

This research was supported by NASA grant Nos. 80NSSC21K1177 and 80NSSC22K0064. This paper makes use of the following ALMA data: ADS/JAO.ALMA#2017.1.00598.S. ALMA is a partnership of the ESO (representing its member states), NSF (USA), and NINS (Japan), together with NRC (Canada), MOST and ASIAA (Taiwan), and KASI (Republic of Korea), in cooperation with the Republic of Chile. The Joint ALMA Observatory is operated by ESO, AUI/NRAO, and NAOJ. The National Radio Astronomy Observatory is a facility of the National Science Foundation operated under cooperative agreement by Associated Universities, Inc. M.A.J. gratefully acknowledges financial support for this research by the Fulbright U.S. Student Program, which is sponsored by the U.S. Department of State and U.S.-Chile Fulbright Commission. Its contents are solely the responsibility of the author and do not necessarily represent the official views of the Fulbright Program, the Government of the United States, or the U.S.-Chile Fulbright Commission. E.T. and F.E.B. gratefully acknowledge funding from ANID programs FONDECYT Regular 1200495, CATA-BASAL FB210003, and Millennium Science Initiative Programs NCN19_058. C.R. acknowledges support from Fondecyt Regular grant No. 1230345 and ANID BASAL project FB210003. J.S.G. thanks the University of Wisconsin College of Letters and Science and Macalester College for partial support of his research on CONs.

Software: ipython (F. Perez & B. E. Granger 2007), numpy (S. Van der Walt et al. 2011), Astropy (Astropy Collaboration et al. 2013), Spectral-Cube (T. Robitaille et al. 2016).

ORCID iDs

Makoto A. Johnstone https://orcid.org/0000-0001-7690-3976
George C. Privon https://orcid.org/0000-0003-3474-1125
Loreto Barcos-Muñoz https://orcid.org/0000-0003-0057-8892
A.S. Evans https://orcid.org/0000-0003-2638-1334
S. Aalto https://orcid.org/0000-0002-5828-7660
Lee Armus https://orcid.org/0000-0003-3498-2973
Franz E. Bauer https://orcid.org/0000-0002-8686-8737
L. Blecha https://orcid.org/0000-0002-2183-1087
J. S. Gallagher https://orcid.org/0000-0001-8608-0408
S. König https://orcid.org/0000-0001-6174-8467
Claudio Ricci https://orcid.org/0000-0001-5231-2645
Ezequiel Treister https://orcid.org/0000-0001-7568-6412
Cosima Eibensteiner https://orcid.org/0000-0002-1185-2810
Kimberly L. Emig https://orcid.org/0000-0001-6527-6954

Kara N. Green https://orcid.org/0009-0002-2049-9470
Devaky Kunneriath https://orcid.org/0000-0002-1568-579X
Jaya Nagarajan-Swenson https://orcid.org/0009-0002-6248-3688
Alejandro Saravia https://orcid.org/0000-0003-4546-3810
Ilsang Yoon https://orcid.org/0000-0001-9163-0064

References

Aalto, S., Garcia-Burillo, S., Muller, S., et al. 2015b, A&A, 574, A85
Aalto, S., Martìn, S., Costagliola, F., et al. 2015a, A&A, 584, A42
Aalto, S., Muller, S., König, S., et al. 2019, A&A, 627, A147
Andrews, B. H., & Thompson, T. A. 2011, ApJ, 727, 97
Armus, L., Mazzarella, J. M., Evans, A. S., et al. 2009, PASP, 121, 559
Astropy Collaboration, Robitaille, T. P., Tollerud, E. J., et al. 2013, A&A, 558, A33
Barcos-Muñoz, L., Aalto, S., Thompson, T. A., et al. 2018, ApJL, 853, L28
Bauer, F. E., Arévalo, P., Walton, D. J., et al. 2015, ApJ, 812, 116
Briggs, D. S. 1995, PhD thesis, New Mexico Institute of Mining and Technology
Cameron, E. 2011, PASA, 28, 128
Carroll, C. M., Ananna, T. T., Hickox, R. C., et al. 2023, ApJ, 950, 127
CASA Team, Bean, B., Bhatnagar, S., et al. 2022, PASP, 134, 114501
Comerón, S., Knapen, J. H., Ramos Almeida, C., & Watkins, A. E. 2021, A&A, 645, A130
Condon, J. J. 1997, PASP, 109, 166
Falstad, N., Aalto, S., König, S., et al. 2021, A&A, 649, A105
Falstad, N., Aalto, S., Mangum, J. G., et al. 2018, A&A, 609, A75
Falstad, N., Hallqvist, F., Aalto, S., et al. 2019, A&A, 623, A29
Feruglio, C., Fiore, F., Piconcelli, E., et al. 2013, A&A, 558, A87
Fluetsch, A., Maiolino, R., Carniani, S., et al. 2019, MNRAS, 483, 4586
Gandhi, P., Annuar, A., Lansbury, G. B., et al. 2017, MNRAS, 467, 4606
García-Burillo, S., Combes, F., Usero, A., et al. 2014, A&A, 567, A125
García-Burillo, S., Combes, F., Usero, A., et al. 2015, A&A, 580, A35
González-Alfonso, E., Armus, L., Carrera, F. J., et al. 2017, PASA, 34, e054
González-Alfonso, E., & Sakamoto, K. 2019, ApJ, 882, 153
Gorski, M. D., Aalto, S., König, S., et al. 2024, A&A, 684, L11
Herrera-Camus, R., Janssen, A., Sturm, E., et al. 2020, A&A, 635, A47
Hopkins, P. F., Hernquist, L., Cox, T. J., & Kereš, D. 2008, ApJS, 175, 356
Hunter, T. R., Indebetouw, R., Brogan, C. L., et al. 2023, PASP, 135, 074501
Imanishi, M., & Nakanishi, K. 2013, AJ, 146, 91
Imanishi, M., Nakanishi, K., & Izumi, T. 2016, ApJL, 822, L10
Imanishi, M., Nguyen, D. D., Wada, K., et al. 2020, ApJ, 902, 99
Iwasawa, K., Ricci, C., Privon, G. C., et al. 2020, A&A, 640, A95
Izumi, T., Kohno, K., Aalto, S., et al. 2015, ApJ, 811, 39
Izumi, T., Kohno, K., Aalto, S., et al. 2016, ApJ, 818, 42
Janssen, A. W., Christopher, N., Sturm, E., et al. 2016, ApJ, 822, 43
Kawamuro, T., Ricci, C., Imanishi, M., et al. 2022, ApJ, 938, 87
Lutz, D., Sturm, E., Janssen, A., et al. 2020, A&A, 633, A134
Martín, S., Aalto, S., Sakamoto, K., et al. 2016, A&A, 590, A25
Mazzolari, G., Gilli, R., Brusa, M., et al. 2024, A&A, 687, A120
Müller-Sánchez, F., Nevin, R., Comerford, J. M., et al. 2018, Natur, 556, 345
Nishimura, Y., Aalto, S., Gorski, M. D., et al. 2024, A&A, 686, A48
Oda, S., Tanimoto, A., Ueda, Y., et al. 2017, ApJ, 835, 179
Oda, S., Ueda, Y., Tanimoto, A., & Ricci, C. 2018, ApJ, 855, 79
Pereira-Santaella, M., Colina, L., García-Burillo, S., et al. 2016, A&A, 594, A81
Pereira-Santaella, M., Colina, L., García-Burillo, S., et al. 2018, A&A, 616, A171
Perez, F., & Granger, B. E. 2007, CSE, 9, 21
Plunkett, A. L., Arce, H. G., Mardones, D., et al. 2015, Natur, 527, 70
Privon, G. C., Aalto, S., Falstad, N., et al. 2017, ApJ, 835, 213
Puccetti, S., Comastri, A., Bauer, F. E., et al. 2016, A&A, 585, A157
Ricci, C., Ananna, T. T., Temple, M. J., et al. 2022, ApJ, 938, 67
Ricci, C., Bauer, F. E., Treister, E., et al. 2016, ApJ, 819, 4
Ricci, C., Bauer, F. E., Treister, E., et al. 2017a, MNRAS, 468, 1273
Ricci, C., Chang, C.-S., Kawamuro, T., et al. 2023, ApJL, 952, L28
Ricci, C., Privon, G. C., Pfeifle, R. W., et al. 2021, MNRAS, 506, 5935
Ricci, C., Trakhtenbrot, B., Koss, M. J., et al. 2017b, ApJS, 233, 17
Ricci, C., Trakhtenbrot, B., Koss, M. J., et al. 2017c, Natur, 549, 488
Ricci, C., Trakhtenbrot, B., Koss, M. J., et al. 2017d, ApJS, 233, 17
Robitaille, T., Ginsburg, A., Beaumont, C., Leroy, A., & Rosolowsky, E., 2016 spectral-cube: Read and analyze astrophysical spectral data cubes, Astrophysics Source Code Library, ascl:1609.017
Sakamoto, K., Aalto, S., Evans, A. S., Wiedner, M. C., & Wilner, D. J. 2010, ApJL, 725, L228
Sakamoto, K., Martín, S., Wilner, D. J., et al. 2021, ApJ, 923, 240
Sanders, D. B., Mazzarella, J. M., Kim, D. C., Surace, J. A., & Soifer, B. T. 2003, AJ, 126, 1607
Scoville, N., Murchikova, L., Walter, F., et al. 2017, ApJ, 836, 66
Solomon, P. M., & Vanden Bout, P. A. 2005, ARA&A, 43, 677
Song, Y., Linden, S. T., Evans, A. S., et al. 2022, ApJ, 940, 52
Teng, S. H., Rigby, J. R., Stern, D., et al. 2015, ApJ, 814, 56
Treister, E., Messias, H., Privon, G. C., et al. 2020, ApJ, 890, 149
Van der Walt, S., Colbert, S. C., & Varoquaux, G. 2011, CSE, 13, 22
Varenius, E., Conway, J. E., Martí-Vidal, I., et al. 2016, A&A, 593, A86
Veilleux, S., Meléndez, M., Sturm, E., et al. 2013, ApJ, 776, 27
Worsley, M. A., Fabian, A. C., Alexander, D. M., et al. 2005, in AIP Conf. Ser. 801, Astrophysical Sources of High Energy Particles and Radiation, ed. T. Bulik, B. Rudak, & G. Madejski (Melville, NY: AIP), 51
Yamada, S., Ueda, Y., Tanimoto, A., et al. 2020, ApJ, 897, 107
Yutani, N., Toba, Y., Baba, S., & Wada, K. 2022, ApJ, 936, 118
Zhao, Y., Lu, N., Xu, C. K., et al. 2016, ApJ, 820, 118
Ziurys, L. M., & Turner, B. E. 1986, ApJL, 300, L19